

University of Nebraska - Lincoln

DigitalCommons@University of Nebraska - Lincoln

Faculty Publications -- Chemistry Department

Published Research - Department of Chemistry

10-10-2019

Reversing Interfacial Catalysis of Ambipolar WSe₂ Single Crystal

Zegao Wang

Sichuan University & Aarhus University

Hong-Hui Wu

University of Nebraska-Lincoln & University of Science and Technology Beijing

Qiang Li

Aarhus University & Shandong University

Flemming Besenbacher

Aarhus University

Yanrong Li

University of Electronic Science and Technology of China

See next page for additional authors

Follow this and additional works at: <https://digitalcommons.unl.edu/chemfacpub>



Part of the [Analytical Chemistry Commons](#), [Medicinal-Pharmaceutical Chemistry Commons](#), and the [Other Chemistry Commons](#)

Wang, Zegao; Wu, Hong-Hui; Li, Qiang; Besenbacher, Flemming; Li, Yanrong; Zeng, Xiao Cheng; and Dong, Mingdong, "Reversing Interfacial Catalysis of Ambipolar WSe₂ Single Crystal" (2019). *Faculty Publications -- Chemistry Department*. 223.

<https://digitalcommons.unl.edu/chemfacpub/223>

This Article is brought to you for free and open access by the Published Research - Department of Chemistry at DigitalCommons@University of Nebraska - Lincoln. It has been accepted for inclusion in Faculty Publications -- Chemistry Department by an authorized administrator of DigitalCommons@University of Nebraska - Lincoln.

Authors

Zegao Wang, Hong-Hui Wu, Qiang Li, Flemming Besenbacher, Yanrong Li, Xiao Cheng Zeng, and Mingdong Dong

Reversing Interfacial Catalysis of Ambipolar WSe₂ Single Crystal

Zegao Wang, Hong-Hui Wu, Qiang Li, Flemming Besenbacher, Yanrong Li, Xiao Cheng Zeng,* and Mingdong Dong*

An improved understanding of the origin of the electrocatalytic activity is of importance to the rational design of highly efficient electrocatalysts for the hydrogen evolution reaction. Here, an ambipolar single-crystal tungsten diselenide (WSe₂) semiconductor is employed as a model system where the conductance and carrier of WSe₂ can be individually tuned by external electric fields. The field-tuned electrochemical microcell is fabricated based on the single-crystal WSe₂ and the catalytic activity of the WSe₂ microcell is measured versus the external electric field. Results show that WSe₂ with electrons serving as the dominant carrier yields much higher activity than WSe₂ with holes serving as the dominant carrier even both systems exhibit similar conductance. The catalytic activity enhancement can be characterized by the Tafel slope decrease from 138 to 104 mV per decade, while the electron area concentration increases from 0.64×10^{12} to $1.72 \times 10^{12} \text{ cm}^{-2}$. To further understand the underlying mechanism, the Gibbs free energy and charge distribution for adsorbed hydrogen on WSe₂ versus the area charge concentration is systematically computed, which is in line with experiments. This comprehensive study not only sheds light on the mechanism underlying the electrocatalysis processes, but also offers a strategy to achieve higher electrocatalytic activity.


1. Introduction

Fossil fuel, as a dominant energy supply, gives rise to environmental pollution and leads to climate change. Therefore, the development of clean and renewable energy is the key way to meet the increasing global energy requirement and to resolve the environmental pollution caused by the overuse of fossil fuels.^[1-3] Hydrogen has been considered as a promising green energy carrier due to its highest energy density and pollution-free and carbon-free production.^[4-6] Generally, the splitting of water by electrocatalysts is regarded as a promising way for hydrogen generation.^[7] The key to realizing this reaction is to find an efficient and robust electrocatalyst which can effectively lower the reaction barrier and result in highly efficient utilization of electric.^[8]

Prof. Z. Wang
College of Materials Science and Engineering
Sichuan University
Chengdu 610065, China

Prof. Z. Wang, Prof. Q. Li, Prof. F. Besenbacher, Prof. M. Dong
Interdisciplinary Nanoscience Center (iNANO)
Aarhus University
DK-8000, Aarhus C, Denmark
E-mail: dong@inano.au.dk

Dr. H.-H. Wu, Prof. X. C. Zeng
Department of Chemistry
University of Nebraska-Lincoln
NE 68588, Lincoln, USA
E-mail: xzeng1@unl.edu

 The ORCID identification number(s) for the author(s) of this article can be found under <https://doi.org/10.1002/advs.201901382>.

© 2019 Aarhus University/iNANO Center. Published by WILEY-VCH Verlag GmbH & Co. KGaA, Weinheim. This is an open access article under the terms of the Creative Commons Attribution License, which permits use, distribution and reproduction in any medium, provided the original work is properly cited.

DOI: 10.1002/advs.201901382

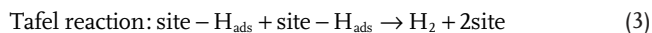
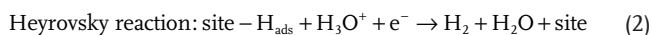
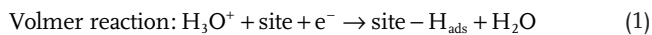
Prof. H.-H. Wu
Beijing Advanced Innovation Center for Materials Genome Engineering
State Key Laboratory for Advanced Metals and Materials
University of Science and Technology Beijing
Beijing 100083, China

Prof. Q. Li
Key Laboratory of Colloid and Interface Chemistry
Ministry of Education
Shandong University
Jinan 250100, China

Prof. Y. Li
State Key Laboratory of Electronic Thin Films and Integrated Devices
University of Electronic Science and Technology of China
Chengdu 610054, China

Prof. X. C. Zeng
Department of Chemical and Biomolecular Engineering and Department of Mechanical and Materials Engineering
University of Nebraska-Lincoln
NE 68588, Lincoln, USA

One key reaction in water splitting is the hydrogen evolution reaction (HER),^[5,9,10] which includes three reactions:



There are two pathways for generating molecular hydrogen, following either Volmer–Heyrovsky reaction or Volmer–Tafel reaction.^[11] Therefore, the Volmer reaction is the key step in HER and it is strongly dependent on the electron transfer, the density of active sites, and the Gibbs free energy of adsorbed atomic hydrogen.^[12–15] To improve these factors, many strategies have been developed, such as improving the catalyst's conductance by introducing a conductive network, increasing the number of active sites by making nanostructure, and modifying materials through element doping or compositing.^[3,4,7,16–18] Among them, the enhancement mechanism through improving conductivity is still unclear, possibly due to the complicated model system with varying factors like active site or nanostructures. Recently, it has been reported that reducing the resistance of catalyst by phase changing or introduction of external field can enhance the catalytic activity as both strategies can facilitate electron injection onto the active sites.^[19–21] Because the external electric field can modify the resistance of semiconductor and the carrier type and concentration, it is hard to distinguish whether the enhanced HER performance is due to enhanced conductance or due to increased electron concentration. Revealing this mechanism not only can further help to understand the enhancement mechanism, but also can help to rationally design of new electrocatalyst with high activity.

However, distinguishing the role of conductance and carrier on the powder-like catalyst is very complicated due to factors such as the uncontrolled defects, nanostructures, and conductance. As an alternative, the high-quality single crystal flake is an ideal model electrocatalyst for fundamental study.^[22] Although the conductance of unipolar semiconductor (n-type or p-type semiconductor) can be tuned by external electric field,^[23] the dominant carrier type could hardly switch between electron and hole. In this study, the ambipolar single-crystal WSe₂ semiconductor is employed as a model electrocatalyst because the conductance of WSe₂ could be effectively tuned, and more importantly, its dominant carrier can be easily switched between hole and electron by external electric field.^[24,25] Therefore, the influence on catalytic activity by conductance or by carrier can be effectively isolated. The ambipolar WSe₂-based electrochemical microcell is constructed. By tuning the external electric field, the catalytic activity can be in situ estimated under the same conductance with the opposite carrier type. This is a good platform to investigate the role of conductance and carrier in the catalytic reaction. The results show that with the similar conductance, WSe₂ with electrons as the dominant carrier exhibits much higher catalytic activity than that of WSe₂ with holes as the dominant carrier. With increasing electron concentration, the catalytic activity is enhanced, as demonstrated by the decrease of Tafel slope from 138 to 104 mV per decade and the

decrease of overpotential at 10 mA cm⁻² from 0.37 to 0.28 V. These results directly demonstrates that the electron carrier concentration plays a more important role in HER. Further, the WSe₂ with different area charge concentration has been studied by using density-functional-theory (DFT) computation. The Gibbs free energy and the charge distribution have been computed, both being in line with our experiment.

2. Results and Discussion

The WSe₂ flake was transferred on SiO₂/Si substrate by mechanical exfoliation. The thickness of WSe₂ was identified according to the optical contrast and AFM morphology measurement. Our previous study demonstrates that the electrical property of WSe₂ is strongly dependent on its thickness, and the WSe₂ flake with 12 layers has the best ambipolar electrical property with the highest carrier mobility.^[24] Therefore, in this study, the WSe₂ flakes with a thickness of 12 layers were selected. The standard electron beam lithography process and followed electron beam evaporation were carried to form the electrical connections. To archive enough space to form an electrolyte droplet, the electrodes are extended to more than 1 cm, locating near the edge of the substrate. Then, PMMA (A11 concentration) was coated and expose the reaction window on the WSe₂ flake by electron beam lithography. It should be noted that the surface of the sample has been fully covered by PMMA except the exposed window. The fabrication schema and corresponding optical images are shown in Figure 1a,b. Figure 1c displays the AFM morphology of the exposed window, where the thickness of the covered PMMA is about 2.3 μm. The high quality of the WSe₂ can be demonstrated by the atomic pattern inset in Figure 1c which is required by lateral force microscopy. The micro-size topographic AFM image is shown in Figure S1a (Supporting Information). There are no PMMA residues and no discontinuities (edges or steps) on the WSe₂ surface, indicating that the catalytic activity should stem from WSe₂ basal plane, rather than from the discontinuities (edges or steps) or the defects. Figure 1d shows the transfer characterization of the WSe₂ transistor where the gate voltage is giving through the back conductive silicon. It is clearly seen that the WSe₂ transistor exhibits the ambipolar transport behavior, where the hole is the dominant carrier for V_{GS} < 0 V and the electron is the dominant carrier for V_{GS} > 0 V.^[24] Further, the transport curve shows a symmetric characterization in both hole and electron branches, indicating the balanced hole and electron conductance. After introducing the 0.5 M H₂SO₄ electrolyte, the source-drain conductance and the gate leakage as a function of gate voltage have no obvious change, suggesting WSe₂ is stable in the electrolyte showing symmetric conductance. The ambipolar transport behavior of WSe₂ is a platform to study the role of the carrier in surface catalysis since WSe₂ could have a similar conductance but with opposite carrier type.

To explore the role of the carrier in surface catalysis, the ambipolar WSe₂ transistor with symmetric conductance was employed to construct an electric field tuned electrochemical microcell, as shown in Figure 2a. In this setup, the surface catalysis was assessed by measuring the water splitting property through HER with employing the WSe₂ as the electrocatalyst.

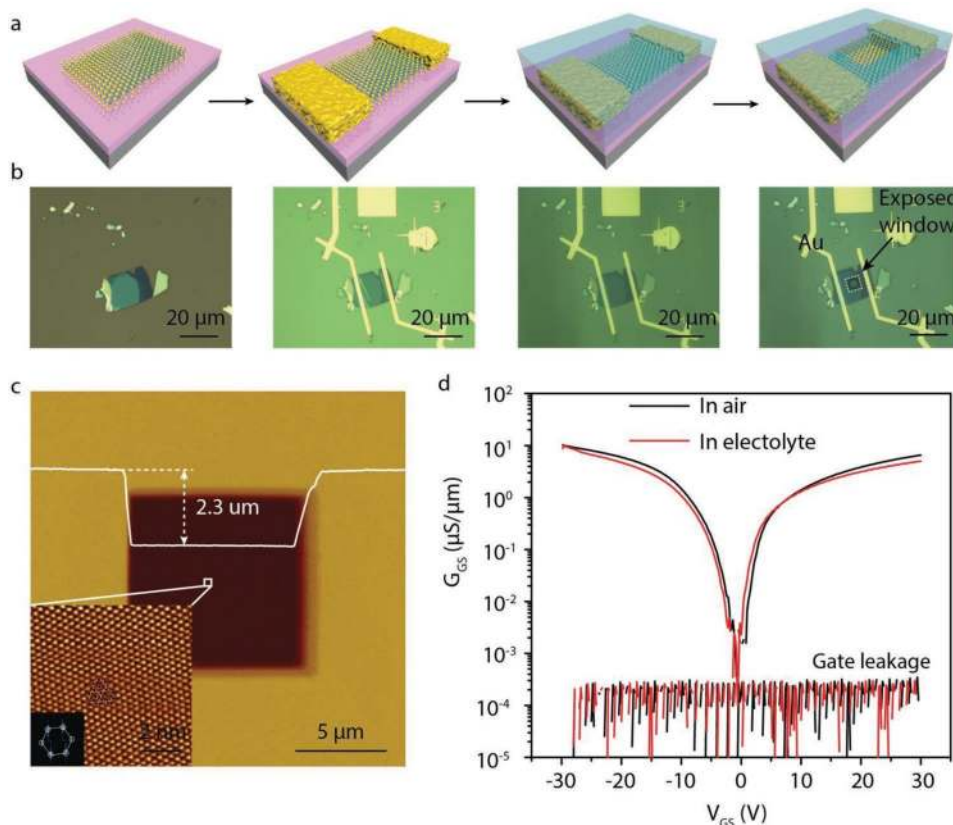


Figure 1. The device fabrication on WSe₂ basal plane. a) A schematic diagram of the fabrication process and b) a realistic optical image of WSe₂ device. c) The AFM height image of the protected PMMA layer, where the window is exposed by EBL only on the WSe₂ basal plane. The inset shows the low pass filtered atomic pattern acquired from the center region by lateral force microscopy. d) The electrical performance of WSe₂ device in the air and an electrolyte. The electrolyte is 0.5 mol L⁻¹ H₂SO₄ solution.

HER is carried out using a three-electrode configuration with Pt wire as the counterelectrode, micro-Ag/AgCl electrode as the reference electrode, and the electrode connected with the WSe₂ flake as the working electrode.^[26] Figure 2b shows the real image of the setup. The transfer curves of the WSe₂ transistor at different conditions (in the air, in the electrolyte and after HER) are shown in Figure 2c. The HER polarization curves (Figure 2d) were measured at different gate voltage corresponding to different carrier envelope. As seen, the WSe₂ flake exhibits a similar conductance ($\approx 3 \mu\text{S} \mu\text{m}^{-1}$) at $V_{\text{GS}} = +10$ and -20 V but with electron and hole as a dominant carrier, respectively. It is surprising that the polarization current at $V_{\text{GS}} = +10$ V can reach about 0.5 A cm^{-2} (when the potential is -0.8 V vs RHE), which is three orders higher than the polarization current at $V_{\text{GS}} = -20$ V. This implies that the conductance of catalysts may not be the key factor in catalytic reaction. The lower polarization current at $V_{\text{GS}} = 0$ V is much lower since WSe₂ is an insulator. The blue line in Figure 2c shows the transport curve after these HER measurements which directly confirm the stability of WSe₂, further confirming that the WSe₂ flake at $V_{\text{GS}} = +10$ and -20 V exhibits the similar conductance but different carrier type. Considering that the solution gate from the counterelectrode has little influence on the electrochemical catalytic reaction,^[21] the enhanced catalytic activity should be originated from the material's property. The topographic AFM image and

Raman spectra of WSe₂ prior to and after the reaction is shown in Figure S1 (Supporting Information). As seen, there are no obvious changes in morphology and Raman spectra, indicating that the WSe₂ basal plane is stable.

The polarization curves of the WSe₂ flake at different gate voltages are shown in Figure 3. The gate voltages are tuned as the sequence of 0, +5, +10, +15, +20, 0, and -20 V. The polarization curves of $V_{\text{GS}} = 0$ V are overlapped excluding the variation of WSe₂ material during the measurement. After all HER measurements, the transfer curve of the WSe₂ transistor in electrolyte still exhibits the symmetric conductance character, meaning the above HER measurements are performed under symmetric transport condition. The carrier concentration could be calculated by $n = C_0(V_{\text{GS}} - V_0)/e$, where n is the carrier concentration, C_0 is the capacity, V_0 is the neutral point, and e is the electron charge.^[27] In this device, the V_0 is about -4 V, possible due to the intrinsic dopant in the WSe₂ crystal. Figure 3b shows the Tafel curves which are fitted according to Tafel equation: $\eta = b \log(j) + a$, where η is the potential, b is the Tafel slope, and j is current density, respectively. The carrier area concentration, conductance, Tafel slope, and overpotential are summarized in Table 1. As seen, the polarization current is largely boosted with the increasing of gate voltage from 0 to $+20$ V. The overpotentials calculated at the polarization current of 10 mA cm^{-2} are 0.37, 0.32, 0.30, and 0.28 V when gate

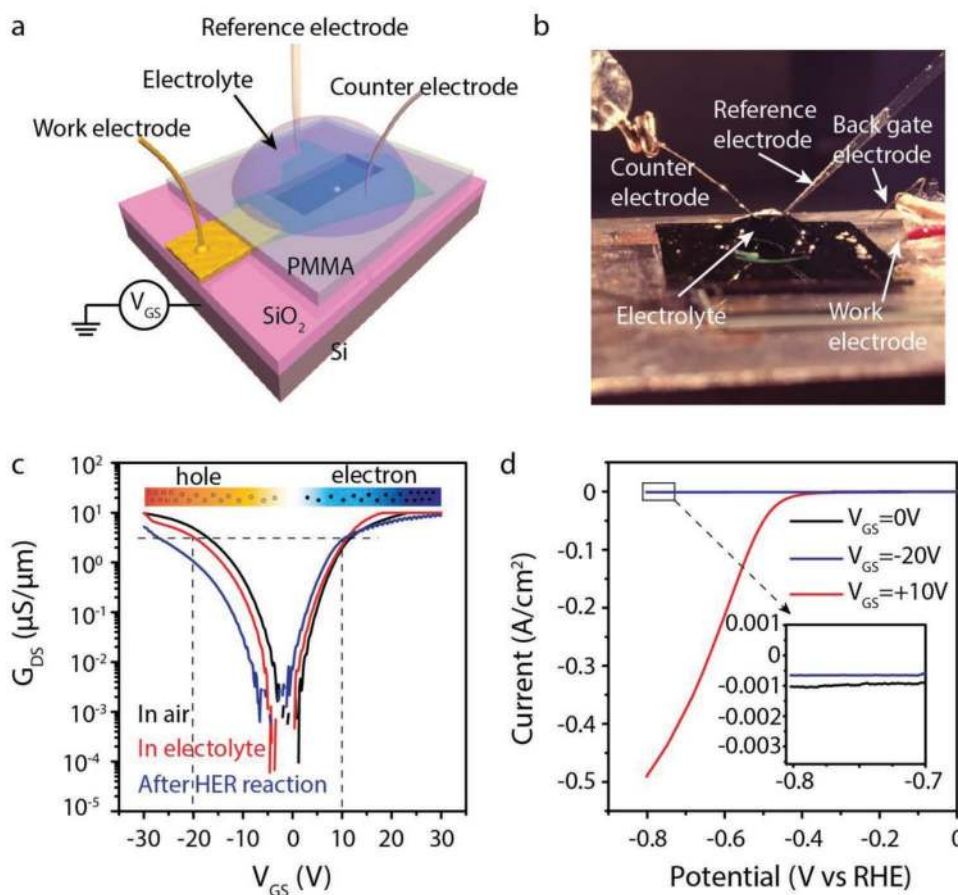


Figure 2. The electrocatalytic performance in electron and hole branches on the ambipolar WSe_2 device. a) A schematic of the setup showing a single gold pad connected with a WSe_2 flake used as the working electrode. b) Photography of the electrochemical microcell. c) The electrical transfer properties of the WSe_2 device in the air, in the electrolyte and after HER reaction, respectively. d) Typical polarization curves measured for the WSe_2 device when the gate voltage is 0, -20, and +10 V, respectively. The electrocatalytic measurement is in 0.5 M H_2SO_4 with a scan ratio of 5 mV s^{-1} . The inset is the corresponding Tafel plot.

voltages are +5, +10, +15, and +20 V, respectively. Even WSe_2 at $V_{\text{GS}} = -20 \text{ V}$ exhibits a higher conductance ($0.932 \mu\text{S } \mu\text{m}^{-1}$) compared with WSe_2 at $V_{\text{GS}} = +5 \text{ V}$ (conductance is $0.174 \mu\text{S } \mu\text{m}^{-1}$), the polarization current at $V_{\text{GS}} = -20 \text{ V}$ is still much lower than that at $V_{\text{GS}} = +5 \text{ V}$, which shows a similar phenomenon with the previous device in Figure 2. During tuning the gate voltage, the carrier concentration and also the conductance are both tuned. However, the conductance of WSe_2 increases from 0.174 to $4.695 \mu\text{S } \mu\text{m}^{-1}$ when the gate voltage increases from +5 to +20 V. Considering that when the resistance is smaller than 10–100 k Ω mm (corresponding to that conductance is higher than 0.01–0.1 $\mu\text{S } \mu\text{m}^{-1}$), the variation of resistance or conductance gives no obvious influence on catalytic activity.^[20,26] Thus, we can propose that the varied catalytic activity (Tafel slope or overpotential) is due to the increased area electron concentration rather than the improved conductance. The results also suggest that the electron carrier is the key factor during electrocatalytic reaction rather than the conductivity, and that synthesis of electron-rich electrocatalyst is preferred. Although the external field modulation may not lead to the highest catalytic performance, combination with other strategies, e.g., introducing point

defects via doping heteroatoms^[28,29] may further enhance the catalytic performance.

The in situ HER measurements are all made under the same condition, for example, the same contact property and the same surface structure. The experimental results indicate that WSe_2 with electrons as the dominant carrier exhibits much higher catalytic activity than that of WSe_2 with holes as the dominant carrier when they have similar conductance. To further understand the underlying mechanism of enhanced HER activity by extra electron or hole, DFT calculation is carried out to evaluate the Gibbs free energy of a hydrogen atom on a charged WSe_2 sheet, a known factor for determining the HER activity. For seeking a starting configuration of the most stable adsorption site, we examine all possible initial positions for H adsorption with symmetry considerations. Figure S2 (Supporting Information) depicts the top and side views of three optimized configurations. The corresponding formation energy is calculated by $E_{\text{formation}} = E_{\text{H+WSe}_2} - E_{\text{H}} - E_{\text{WSe}_2}$, where $E_{\text{H+WSe}_2}$ is the total energy of the H atom adsorbed on the WSe_2 sheet, E_{H} is the energy of the H atom, and E_{WSe_2} is the energy of the WSe_2 sheet. As seen, the hydrogen atom adsorbed on the top of six-ring and near the Se atom (Figure S2c,

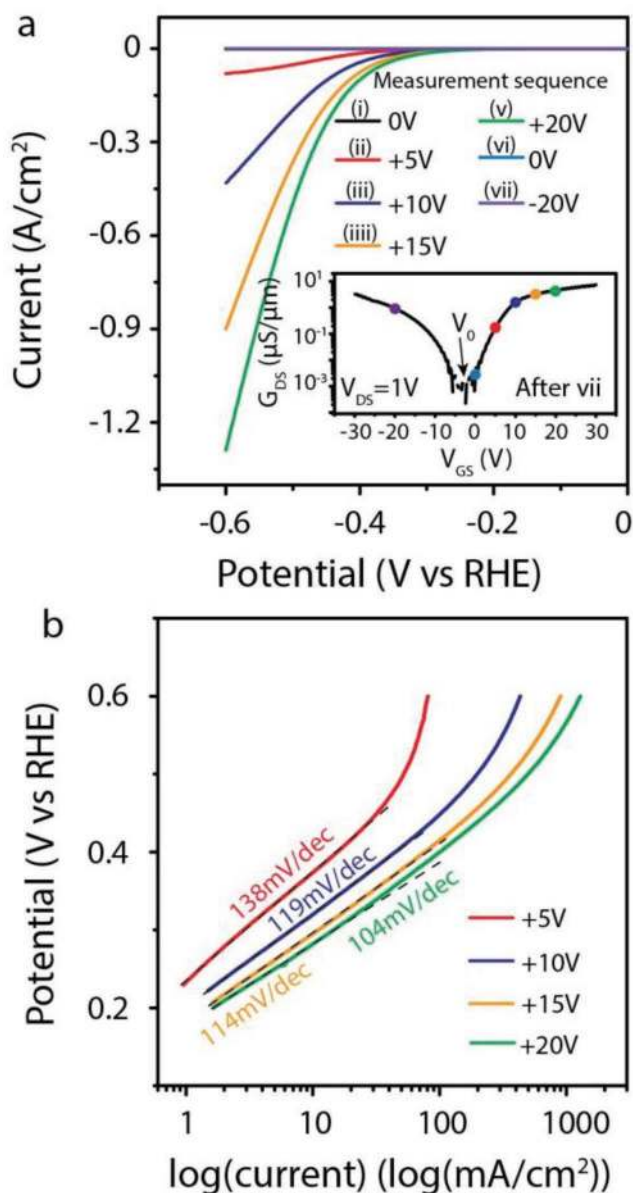


Figure 3. Gate voltage-dependent electrocatalytic activity on the ambipolar WSe₂ device. a) The polarization curves measured under different gate voltages, and the inset shows the electrical transport property of WSe₂ device after all measurements. b) The Tafel plots from (a).

Table 1. The carrier concentration (per unit area), conductance, Tafel slope, and overpotential of WSe₂ electrocatalysts under different gate voltage.

V _{GS} [V]	N [$\times 10^{12}$ cm ⁻²]	G [μ S μ m ⁻¹]	Tafel slope [mV per decade]	Overpotential (at 10 mA cm ⁻² , V vs RHE)
0	-0.29	2.393e-3	-	-
5	-0.64	0.174	138	0.37
10	-1.00	1.595	119	0.32
15	-1.36	3.271	114	0.30
20	-1.72	4.695	104	0.28
-20	+1.15	0.932	-	-

"-": electron carrier; "+": hole carrier.

Supporting Information) is the favorable energy state with the lowest formation energy. Based on the most stable adsorption structure, **Figure 4a–c** shows the optimized WSe₂ sheet with an adsorbed H at different carrier area concentration (n) of 6.45×10^{13} , 0.00, and -2.58×10^{13} cm⁻², respectively. The negative carrier means the carrier is a hole, while the positive carrier means the carrier is an electron. The corresponding carrier concentration varies from 1.94×10^{13} to -2.58×10^{13} cm⁻², calculated based on the area of the model system (1.55×10^{-14} cm²). When the extra carrier of the system is zero, the preferential H position is near a Se atom, where a Se–H bond is formed.

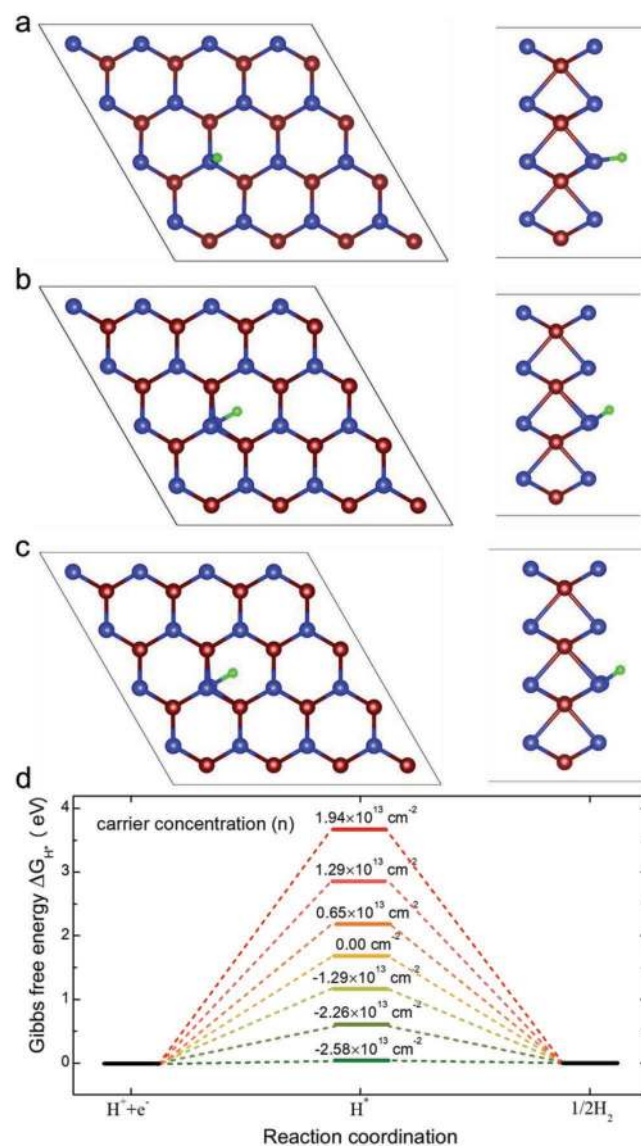


Figure 4. DFT calculation results of hydrogen atom adsorbed on charged WSe₂ sheet with respect to the different carrier concentration (per unit area n). The associated adsorption sites at $n =$ a) 0.65×10^{13} cm⁻², b) neutral, and c) -2.58×10^{13} cm⁻². d) The Gibbs free-energy diagram of hydrogen evolution reaction. The blue, purple and green balls represent Se, W, and H atoms, respectively. The $n > 0$ corresponds to the added hole in the system, while $n < 0$ corresponds to the added electron in the system.

Interestingly, the position of the adsorbed H with respect to the Se atom depends on its charge state. In the neutral and negative charge states, the H is located at the antibonding site, as shown in Figure 4b,c. The Se–H bond is aligned with a W–Se bond, pointing toward the surface spacing.

The preferential position of the adsorbed H in the positive charge state is different, where the adsorbed H moves toward the top of a Se atom (Figure 4a). A similar adsorption site of H was reported in MoS₂.^[28,29] Generally, a good HER catalyst should feature $|\Delta G_{\text{H}^*}|$ value near zero, which allows optimal adsorption/desorption kinetics. Further atomic insight into the carrier-induced HER activity differences is obtained from the computed adsorption Gibbs free energy of the bonded hydrogen atom. The calculated free energy is illustrated in Figure 4d. In the cases of the extra holes, the ΔG_{H^*} values are too positive, and the H* species cannot be adsorbed onto the catalyst surface, and thus they are also unsuitable for HER. Compared with the pristine WSe₂ structure without an extra carrier, the extra electrons lead to more negative ΔG_{H^*} values, indicating a more favorable adsorption process for the H* species. When the extra electron area concentration is $-2.58 \times 10^{13} \text{ cm}^{-2}$, the catalyst exhibits a desired ΔG_{H^*} value of 0.033 eV, which is closer to zero than that of the well-known Pt-based catalyst ($|\Delta G_{\text{H}^*}| = 0.09 \text{ eV}$).^[30–32] The basic trend of our theoretical results is qualitatively consistent with that of experimental results, even though the specific values are not exactly the same. We examine the effects of spin polarization and the use of different pseudopotential in our DFT calculations. As shown in Figures S4 and S5 (Supporting Information), neither the spin nor the GBRV pseudopotential can have much influence on the variation trends of the free energy, indicating the reliability of the current DFT calculation results. To gain a deeper understanding of the experimental results, we also examine the role of defect sites in the catalytic reaction (see Figures S6 and S7 in the Supporting Information). Both W point defects and edge defects can decrease the Gibbs free energy to a certain level, depending on the position relative to the defect site, whereas the Se vacancy can increase the Gibbs free energy. The opposing effects of the defects on the Gibbs free energy suggest that the defects alone cannot explain the experimental results of increased HER activity. Alternatively, we find that the HER activity is very localized to the adsorption site, suggesting that the system area in the DFT calculation plays a decisive role in the electron area concentration. Besides the system size of $4 \times 4 \times 1$ supercell, we also consider a larger supercell size with $8 \times 8 \times 1$ unit cells (193 atoms) to illustrate this point. As shown in Figure S8 (Supporting Information), the larger supercell results in reduced electron area concentration to nearly one eighth. It is known that Gibbs free energy ΔG_{H^*} is a commonly used descriptor for characterizing the catalytic activity of H atom adsorption. Some other important descriptors for understanding the structure-activity-selectivity relationships include the electronic level, i.e., electron charge, valance band position, etc.^[28]

The difference in the H atomic position and the interaction between H atom and the WSe₂ sheet cause distinct charge transfer behaviors. To correlate this charge transfer behavior with the HER activity, we construct the charge-difference plot, where the charge difference is calculated by

$\Delta\rho = \rho_{\text{H+WSe}_2} - \rho_{\text{H}} - \rho_{\text{WSe}_2}$. Here, $\rho_{\text{H+WSe}_2}$ is the total charge density of the H atom adsorbed on the WSe₂ sheet, ρ_{H} is the charge density of the H atom, and ρ_{WSe_2} is the charge density of the WSe₂ sheet.^[33] Figure 5a–d present the WSe₂ sheet adsorbed with one H atom with respect to different carrier area concentration 6.45×10^{13} , 3.22×10^{13} , 0.00, and $-2.58 \times 10^{13} \text{ cm}^{-2}$, respectively. Similar to the reported MoS₂ for HER process,^[16,26,34] because of the very high level of 3p orbital with respect to the H 1s orbital, the H adsorption on the basal plane of pristine WSe₂ is too weak ($\Delta G_{\text{H}^*} = 1.68 \text{ eV}$), leading to a poor HER performance. As shown in Figure 5a–d, when the extra carrier is a hole, the hydrogen atom is surrounded by the electron depletion region, as denoted by Figure 4e, which is unfavorable for HER activity. With the extra electron increasing from 0.00 to $-2.58 \times 10^{13} \text{ cm}^{-2}$, it will strengthen the adsorption and change the charge state of H atom from electron depletion to electron accumulation, which offsets the energy level for enhancing the H adsorption and HER activity. However, with the area concentration of extra electron further increasing, the further enhanced adsorption energy would render the desorption process difficult, and thus deteriorate the HER performance. In other words, the extra electron carrier would contribute to the charge redistribution with the decrease of adsorption energy. A suitable amount of electrons would lead to favorable adsorption/desorption of H atoms for high-performance HER. To illustrate in detail the nature of charge transfer behavior, the plane averaged carrier concentration along the out-of-plane direction is shown in Figure 5e. The plane averaged carrier concentration is calculated by $\Delta\sigma(z) = \sigma_{\text{H+WSe}_2}(z) - \sigma_{\text{H}}(z) - \sigma_{\text{WSe}_2}(z)$, where $\sigma_{\text{H+WSe}_2}(z)$ is plane averaged charge density of the combined H–WSe₂ system, $\sigma_{\text{H}}(z)$ and $\sigma_{\text{WSe}_2}(z)$ are, respectively, the plane averaged charge density of the isolated H atom and WSe₂ layer, which are calculated by fixing the atomic positions of the corresponding components in the combined system. The positive and negative values indicate charge loss and gain, respectively. It is clear that the extra electron contributes to a smoother distribution of charge, which attributes to the higher mobility of extra electron. However, the hole carrier causes a more localized charge transfer. Both the charge depletion and charge accumulation constitute the charge redistribution behavior, and ultimately, affect the hydrogen adsorption. The DFT calculation demonstrates that the hole carrier or overly introduced electron carrier can induce too positive or too negative Gibbs free energy, neither favorable to the adsorption and desorption of hydrogen atom. An appropriate area concentration of electron carrier would give rise to optimal Gibbs free energy, closer to the value of Pt.

3. Conclusion

In summary, the role of the carrier on catalytic activity has been systemically studied from experiment and DFT calculation. The ambipolar WSe₂-based electrochemical microcell provides the platform to estimate the in situ catalytic activity under the same condition (defect, active site, nanostructure, etc.). With varying the external field, the dominant carrier in WSe₂ can switch between electron and hole, while the conductance of WSe₂ can be tuned as well. The effect of the electron carrier, hole carrier,

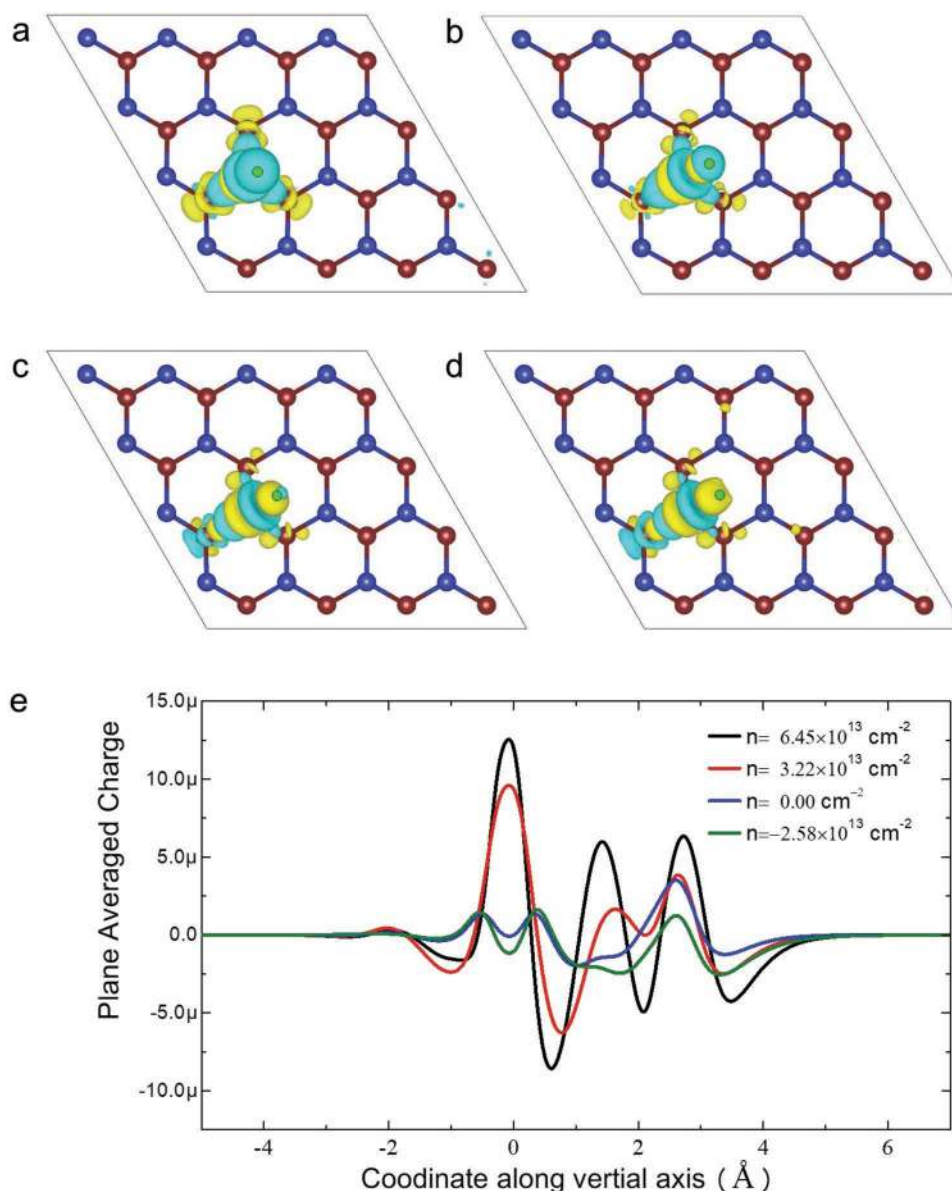


Figure 5. The charge difference plot of the hydrogen atom adsorbed on the charged WSe_2 sheet with different carrier concentration (per unit area n): a) $n = 6.45 \times 10^{13} \text{ cm}^{-2}$; b) $n = 3.22 \times 10^{13} \text{ cm}^{-2}$; c) $n = 0.00 \text{ cm}^{-2}$; and d) $n = -2.58 \times 10^{13} \text{ cm}^{-2}$. The isovalue is $0.0025 \text{ e Bohr}^{-3}$. The yellow region indicates electron accumulation, and the cyan region indicates electron depletion, respectively. The H atom is highlighted by a black circle. e) The plane averaged carrier concentration along the out-of-plane direction when the WSe_2 has a different charge density.

and conductance in catalysis reaction has been carefully discussed. The results show that with the similar conductance, WSe_2 with the electrons as the dominant carrier shows much higher catalytic activity than that with the holes as the dominant carrier. With increasing the gate voltage in electron dominated WSe_2 , the catalytic activity can be further enhanced with the Tafel slope decreasing from 138 to 104 mV per decade, attributing to the increased electron concentration rather than the conductance. Furthermore, the Gibbs free energies of adsorbed atomic hydrogen on WSe_2 with different electron and hole area concentrations are calculated. The results show that ΔG_{H^*} of electron dominated WSe_2 is much lower than that of hole dominated WSe_2 . Moreover, the ΔG_{H^*} can be lowered to 0.033 from

1.68 eV by injecting electrons into pristine WSe_2 with an electron area concentration of $2.58 \times 10^{13} \text{ cm}^{-2}$. The results show that the electron carrier plays a more important role in HER, rather than the conductance, which provides a new strategy to rationally design highly efficient electrocatalysts.

4. Experimental Section

Device Fabrication and Measurement: The WSe_2 flakes were mechanically exfoliated from a bulk crystal onto a SiO_2/Si substrate with a size of $2 \text{ cm} \times 2 \text{ cm}$. The WSe_2 flake with a thickness of 12 layers, which exhibits the highest carrier mobility and ambipolar behavior,^[24] is selected. The source and drain electrodes were patterned with electron

beam lithography. Then 10 nm Ti/40 nm Au layers were evaporated by electron beam deposition with a depositing speed of 0.2 \AA s^{-1} . Before evaporation, the sample was kept overnight under the high vacuum in the electron beam deposition system. To have enough space to form an electrolyte droplet, the source and drain electrodes were extended to near the edge of the substrate with a length of about 1 cm. A second electron beam lithography process was employed to expose the basal plane of WSe_2 . To fully cover the WSe_2 edges and the electrodes, PMMA with a concentration of 11% in anisole was spin-coated on the sample and then a conductive polymer was coated on its surface to eliminate the charge effect during electron beam lithography. More attention was devoted to ensuring that no gold electrode and WSe_2 edge were exposed to the electrolyte. After opening the window on the WSe_2 flake, the sample was baked at $180 \text{ }^\circ\text{C}$ for 10 min. The electrical transport property of WSe_2 transistor was carried by Keithley 4200 SCS, and the field tuned electrochemical reaction was performed on electrochemical workstation combined with Keithley 4200 SCS. Linear sweep voltammetry with a scan rate of 5 mV s^{-1} was conducted in $0.5 \text{ M H}_2\text{SO}_4$ solution, using a Pt wire as the counterelectrode. The micro-reference electrode was calibrated for the reversible hydrogen potential, where $E(\text{vs RHE}) = E(\text{vs Ag/AgCl}) + 0.197 \text{ V}$. Before measurement, the H_2SO_4 solution was degassed using pure Ar gas.

Computation: DFT calculations were carried out using the Hartwigsen–Goedecker–Hutter norm-conserving pseudopotentials^[35] and the Perdew–Burke–Ernzerhof (PBE) exchange–correlation functional^[36] as implemented in the Quantum ESPRESSO package.^[37,38] The spin-polarized calculation was employed,^[39] and the vdW + DF2 functional was selected to account for van der Waals (vdW) interactions.^[40] The model system is a 4×4 supercell of WSe_2 (with 48 atoms) and a single hydrogen atom adsorbed on the surface. In the direction vertical to the surface, the supercell extends with a vacuum space for 30 \AA . The Brillouin zone is sampled using a $3 \times 3 \times 1$ Monkhorst–Pack k -point grid. Atomic positions are optimized until the maximum force on all atoms is less than 0.001 a.u. Cutoffs of 40 and 160 Ry were chosen for the wave function and the electronic density, respectively. For the computational scheme based on pseudopotential and periodic slab geometry, it is challenging to deal with the charged system when imposing the periodic boundary condition in the surface normal direction.^[41,42] In the case of the system with the extra carrier, an effective screening medium method (ESM)^[42,43] was utilized to treat effectively charged slabs. ESM screens the electronic charge of a polarized/charged medium along one perpendicular direction by introducing a classical charge model and a local relative permittivity into the DFT calculation framework. In this condition, excess or deficit charge is accommodated on one side of a slab, and the image charge is automatically induced in the medium. Thus, this permits calculation by using open boundary conditions. Lastly, for DFT calculation with a larger supercell with $8 \times 8 \times 1$ unit cells (193 atoms), the Gamma point was adopted.

Supporting Information

Supporting Information is available from the Wiley Online Library or from the author.

Acknowledgements

Z.W. and H.H.W. contributed equally to this work. This research was supported by grants from the Danish National Research Foundation, AUFF-NOVA project from Aarhus Universitets Forskningsfond, and EU H2020RISE 2016-MNR4S Cell project. H. H. Wu acknowledges the financial support from the Natural Science Foundations of China (51901013). X. C. Zeng was supported by UNL Holland Computing Center. Z. Wang was supported by Fundamental Research Funds for the Central Universities, China (YJ201893), and State Key Lab of Advanced Metals and Materials, China (Grant No. 2019-Z03).

Conflict of Interest

The authors declare no conflict of interest.

Keywords

ambipolar carrier, density function theory, electrochemical microcells, hydrogen evolution, model catalysis

Received: June 6, 2019

Revised: October 10, 2019

Published online:

- [1] M. R. Nellist, F. A. L. Laskowski, J. Qiu, H. Hajibabaei, K. Sivula, T. W. Hamann, S. W. Boettcher, *Nat. Energy* **2018**, *3*, 46.
- [2] B. Song, S. Jin, *Joule* **2017**, *1*, 220.
- [3] H. Li, C. Tsai, A. L. Koh, L. Cai, A. W. Contryman, A. H. Fragapane, J. Zhao, H. S. Han, H. C. Manoharan, F. Abild-Pedersen, J. K. Nørskov, X. Zheng, *Nat. Mater.* **2016**, *15*, 48.
- [4] J. Hu, B. Huang, C. Zhang, Z. Wang, Y. An, D. Zhou, H. Lin, M. K. H. Leung, S. Yang, *Energy Environ. Sci.* **2017**, *10*, 593.
- [5] D. Merki, X. Hu, *Energy Environ. Sci.* **2011**, *4*, 3878.
- [6] H. Xu, D. Cheng, D. Cao, X. C. Zeng, *Nat. Catal.* **2018**, *1*, 339.
- [7] J. Miao, F.-X. Xiao, H. B. Yang, S. Y. Khoo, J. Chen, Z. Fan, Y.-Y. Hsu, H. M. Chen, H. Zhang, B. Liu, *Sci. Adv.* **2015**, *1*, e1500259.
- [8] D. Voiry, H. S. Shin, K. P. Loh, M. Chhowalla, *Nat. Rev. Chem.* **2018**, *2*, 0105.
- [9] J. Xie, H. Zhang, S. Li, R. Wang, X. Sun, M. Zhou, J. Zhou, X. W. Lou, Y. Xie, *Adv. Mater.* **2013**, *25*, 5807.
- [10] D. Voiry, J. Yang, M. Chhowalla, *Adv. Mater.* **2016**, *28*, 6197.
- [11] G. Zhao, K. Rui, S. X. Dou, W. Sun, *Adv. Funct. Mater.* **2018**, *28*, 1803291.
- [12] T. Su, Q. Shao, Z. Qin, Z. Guo, Z. Wu, *ACS Catal.* **2018**, *8*, 2253.
- [13] Y. Ying, Z. Yumin, G. Tangling, Y. Tai, Z. Xinghong, H. Jiecai, W. Xianjie, Z. Zhihua, X. Ping, Z. Peng, C. Xingzhong, S. Bo, J. Song, *Adv. Mater.* **2017**, *29*, 1700311.
- [14] Z. Wang, Q. Li, F. Besenbacher, M. Dong, *Adv. Mater.* **2016**, *28*, 10224.
- [15] Q. Liu, Q. Fang, W. Chu, Y. Wan, X. Li, W. Xu, M. Habib, S. Tao, Y. Zhou, D. Liu, T. Xiang, A. Khalil, X. Wu, M. Chhowalla, P. M. Ajayan, L. Song, *Chem. Mater.* **2017**, *29*, 4738.
- [16] J. Deng, H. Li, S. Wang, D. Ding, M. Chen, C. Liu, Z. Tian, K. S. Novoselov, C. Ma, D. Deng, X. Bao, *Nat. Commun.* **2017**, *8*, 14430.
- [17] J. Pető, T. Ollár, P. Vancsó, Z. I. Popov, G. Z. Magda, G. Dobrik, C. Hwang, P. B. Sorokin, L. Tapasztó, *Nat. Chem.* **2018**, *10*, 1246.
- [18] Z. Luo, Y. Ouyang, H. Zhang, M. Xiao, J. Ge, Z. Jiang, J. Wang, D. Tang, X. Cao, C. Liu, W. Xing, *Nat. Commun.* **2018**, *9*, 2120.
- [19] W. Junhui, Y. Mengyu, Z. Kangning, L. Xiaobin, W. Peiyao, P. Xuelei, Y. Wei, M. Liqiang, *Adv. Mater.* **2017**, *29*, 1604464.
- [20] D. Voiry, R. Fullon, J. Yang, C. de Carvalho Castro e Silva, R. Kappera, I. Bozkurt, D. Kaplan, M. J. Lagos, P. E. Batson, G. Gupta, Aditya D. Mohite, L. Dong, D. Er, V. B. Shenoy, T. Asefa, M. Chhowalla, *Nat. Mater.* **2016**, *15*, 1003.
- [21] M. Yan, X. Pan, P. Wang, F. Chen, L. He, G. Jiang, J. Wang, J. Z. Liu, X. Xu, X. Liao, J. Yang, L. Mai, *Nano Lett.* **2017**, *17*, 4109.
- [22] D. Guo, R. Shibuya, C. Akiba, S. Saji, T. Kondo, J. Nakamura, *Science* **2016**, *351*, 361.
- [23] C. Kim, I. Moon, D. Lee, M. S. Choi, F. Ahmed, S. Nam, Y. Cho, H.-J. Shin, S. Park, W. J. Yoo, *ACS Nano* **2017**, *11*, 1588.
- [24] Z. Wang, Q. Li, Y. Chen, B. Cui, Y. Li, F. Besenbacher, M. Dong, *NPG Asia Mater.* **2018**, *10*, 703.

- [25] C. Zhou, Y. Zhao, S. Raju, Y. Wang, Z. Lin, M. Chan, Y. Chai, *Adv. Funct. Mater.* **2016**, *26*, 4223.
- [26] Z. Wang, Q. Li, H. Xu, C. Dahl-Petersen, Q. Yang, D. Cheng, D. Cao, F. Besenbacher, J. V. Lauritsen, S. Helveg, M. Dong, *Nano Energy* **2018**, *49*, 634.
- [27] Z. Wang, H.-H. Wu, Q. Li, F. Besenbacher, X. C. Zeng, M. Dong, *Nanoscale* **2018**, *10*, 18178.
- [28] P. Vancsó, Z. I. Popov, J. Pető, T. Ollár, G. Dobrik, J. S. Pap, C. Hwang, P. B. Sorokin, L. Tapasztó, *ACS Energy Lett.* **2019**, *4*, 1947.
- [29] Y. Shi, Y. Zhou, D. R. Yang, W. X. Xu, C. Wang, F. B. Wang, J. J. Xu, X. H. Xia, H. Y. Chen, *J. Am. Chem. Soc.* **2017**, *139*, 15479.
- [30] J. K. Nørskov, T. Bligaard, A. Logadottir, J. R. Kitchin, J. G. Chen, S. Pandelov, U. Stimming, *J. Electrochem. Soc.* **2005**, *152*, J23.
- [31] Z. Pei, J. Gu, Y. Wang, Z. Tang, Z. Liu, Y. Huang, Y. Huang, J. Zhao, Z. Chen, C. Zhi, *ACS Nano* **2017**, *11*, 6004.
- [32] S. Yu, Y.-C. Rao, H.-H. Wu, X.-M. Duan, *Phys. Chem. Chem. Phys.* **2018**, *20*, 27970.
- [33] W. Tang, E. Sanville, G. Henkelman, *J. Phys. Condens. Matter* **2009**, *21*, 084204.
- [34] C. Tsai, F. Abild-Pedersen, J. K. Nørskov, *Nano Lett.* **2014**, *14*, 1381.
- [35] C. Hartwigsen, S. Goedecker, J. Hutter, *Phys. Rev. B* **1998**, *58*, 3641.
- [36] J. P. Perdew, K. Burke, M. Ernzerhof, *Phys. Rev. Lett.* **1996**, *77*, 3865.
- [37] P. Giannozzi, O. Andreussi, T. Brumme, O. Bunau, M. B. Nardelli, M. Calandra, R. Car, C. Cavazzoni, D. Ceresoli, M. Cococcioni, N. Colonna, I. Carnimeo, A. D. Corso, S. d. Gironcoli, P. Delugas, J. R. A. DiStasio, A. Ferretti, A. Floris, G. Fratesi, G. Fugallo, R. Gebauer, U. Gerstmann, F. Giustino, T. Gorni, J. Jia, M. Kawamura, H. Y. Ko, A. Kokalj, E. Küçükbenli, M. Lazzeri, M. Marsili, N. Marzari, F. Mauri, N. L. Nguyen, H. V. Nguyen, A. Otero-de-la-Roza, L. Paulatto, S. Poncé, D. Rocca, R. Sabatini, B. Santra, M. Schlipf, A. P. Seitsonen, A. Smogunov, I. Timrov, T. Thonhauser, P. Umari, N. Vast, X. Wu, S. Baroni, *J. Phys. Condens. Matter* **2017**, *29*, 465901.
- [38] G. Paolo, B. Stefano, B. Nicola, C. Matteo, C. Roberto, C. Carlo, C. Davide, L. C. Guido, C. Matteo, D. Ismaila, C. Andrea Dal, G. de Stefano, F. Stefano, F. Guido, G. Ralph, G. Uwe, G. Christos, K. Anton, L. Michele, M.-S. Layla, M. Nicola, M. Francesco, M. Riccardo, P. Stefano, P. Alfredo, P. Lorenzo, S. Carlo, S. Sandro, S. Gabriele, P. S. Ari, S. Alexander, U. Paolo, M. W. Renata, *J. Phys. Condens. Matter* **2009**, *21*, 395502.
- [39] H.-H. Wu, H. Huang, J. Zhong, S. Yu, Q. Zhang, X. C. Zeng, *Nanoscale* **2019**, *11*, 12210.
- [40] S. Grimme, *J. Comput. Chem.* **2006**, *27*, 1787.
- [41] G. Makov, M. C. Payne, *Phys. Rev. B* **1995**, *51*, 4014.
- [42] M. Otani, O. Sugino, *Phys. Rev. B* **2006**, *73*, 115407.
- [43] I. Hamada, Y. Morikawa, *J. Phys. Chem. C* **2008**, *112*, 10889.